AD-A181 333   PHASE SCINTILLATION UNDER WEAK AND STRONG SCATTER   1/1
               CONDITIONS(U) SRI INTERNATIONAL MENLO PARK CA
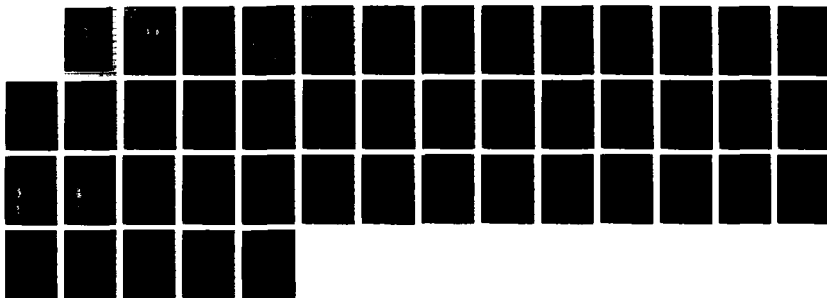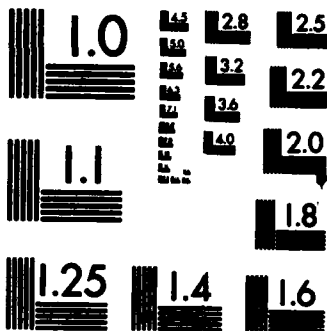   R C LIVINGSTON ET AL. 30 SEP 86 DNA-TR-86-333
UNCLASSIFIED   DNA001-85-C-0062   F/G 20/14   NL

MICROCOPY RESOLUTION TEST CHART
NATIONAL BUREAU OF STANDARDS-1963-A

⑫

DNA-TR-86-333

PHASE SCINTILLATION UNDER WEAK AND STRONG SCATTER CONDITIONS

R. C. Livingston
T. M. Dabbs
SRI International
333 Ravenswood Avenue
Menlo Park, CA 94025-3434

30 September 1986

Technical Report

DTIC
SELECTE
JUN 1 8 1987
D
D

Approved for public release;
distribution is unlimited.

AD-A181 333

Prepared for
   Director
   DEFENSE NUCLEAR AGENCY
   Washington, DC 20305-1000

87 6 16 030

DISTRIBUTION LIST UPDATE

This mailer is provided to enable DNA to maintain current distribution lists for reports. We would appreciate your providing the requested information.

☐   Add the individual listed to your distribution list.

☐   Delete the cited organization/individual.

☐   Change of address.

NAME: _____

ORGANIZATION: _____

OLD ADDRESS	CURRENT ADDRESS
_____	_____
_____	_____
_____	_____

TELEPHONE NUMBER: _(___)_____

SUBJECT AREA(s) OF INTEREST:

_____   _____

_____   _____

_____   _____

DNA OR OTHER GOVERNMENT CONTRACT NUMBER: _____

CERTIFICATION OF NEED-TO-KNOW BY GOVERNMENT SPONSOR (if other than DNA):

SPONSORING ORGANIZATION: _____

CONTRACTING OFFICER OR REPRESENTATIVE: _____

SIGNATURE: _____

CUT HERE AND RETURN

Director
Defense Nuclear Agency
ATTN: ███ TITL
Washington, DC 20305-1000

REPORT DOCUMENTATION PAGE

1a. REPORT SECURITY CLASSIFICATION UNCLASSIFIED		1b. RESTRICTIVE MARKINGS *AI81333*
2a. SECURITY CLASSIFICATION AUTHORITY N/A since Unclassified		3. DISTRIBUTION/AVAILABILITY OF REPORT Approved for public release; distribution is unlimited.
2b. DECLASSIFICATION/DOWNGRADING SCHEDULE N/A since Unclassified		
4. PERFORMING ORGANIZATION REPORT NUMBER(S) SRI Project 8390		5. MONITORING ORGANIZATION REPORT NUMBER(S) DNA-TR-86-333
6a. NAME OF PERFORMING ORGANIZATION SRI International	6b. OFFICE SYMBOL (If applicable)	7a. NAME OF MONITORING ORGANIZATION Director Defense Nuclear Agency
6c. ADDRESS (City, State, and ZIP Code) 333 Ravenswood Avenue Menlo Park, California 94025-3434		7b. ADDRESS (City, State, and ZIP Code) Washington, DC 20305-1000
8a. NAME OF FUNDING/SPONSORING ORGANIZATION	8b. OFFICE SYMBOL (If applicable) RAAE/Wittwer	9. PROCUREMENT INSTRUMENT IDENTIFICATION NUMBER DNA 001-85-C-0062

8c. ADDRESS (City, State, and ZIP Code)	10. SOURCE OF FUNDING NUMBERS			
	PROGRAM ELEMENT NO. 62715H	PROJECT NO. RB	TASK NO. RX	WORK UNIT ACCESSION NO. DH008710

11. TITLE (Include Security Classification)

PHASE SCINTILLATION UNDER WEAK AND STRONG SCATTER CONDITIONS

12. PERSONAL AUTHOR(S)
Livingston, Robert C. and Dabbs, Teri M.

13a. TYPE OF REPORT Technical	13b. TIME COVERED FROM 850313 TO 860930	14. DATE OF REPORT (Year, Month, Day) 860930	15. PAGE COUNT 44

16. SUPPLEMENTARY NOTATION
This work was sponsored by the Defense Nuclear Agency under RDT&E RMC Code B3220854693 RB RX 00002 25904D.

17. COSATI CODES			18. SUBJECT TERMS (Continue on reverse if necessary and identify by block number)
FIELD	GROUP	SUB-GROUP	Radio Wave Scintillation Strong Scatter
17	02	1	Weak Scatter Diffraction Effects
20	09		

19. ABSTRACT (Continue on reverse if necessary and identify by block number)

Equatorial observations from the DNA Wideband satellite have been analyzed to: (1) characterize the two-component phase spectral form, and (2) estimate the effects of diffraction on the phase spectrum during strong scatter conditions. The average two-component phase spectrum has a low frequency dependence of $f^{-2.3}$, and $f^{-3.9}$ at high frequencies. These regimes are separated by a spectral break at ~650 m. For weak scatter levels up to $S_4 \leq 0.5$, diffraction errors are less than one radian, and phase spectral shape is independent of carrier frequency. At higher S_4 values, the

20. DISTRIBUTION/AVAILABILITY OF ABSTRACT ☐ UNCLASSIFIED/UNLIMITED ☒ SAME AS RPT. ☐ DTIC USERS	21. ABSTRACT SECURITY CLASSIFICATION UNCLASSIFIED	
22a. NAME OF RESPONSIBLE INDIVIDUAL Sandra E. Young	22b. TELEPHONE (Include Area Code) (202) 325-7042	22c. OFFICE SYMBOL DNA/CSTI

DD FORM 1473, 84 MAR   83 APR edition may be used until exhausted.   SECURITY CLASSIFICATION OF THIS PAGE
                                  All other editions are obsolete.

UNCLASSIFIED

19. ABSTRACT (Continued)

spectrum is affected by diffraction at all spatial frequencies and its shape depends on carrier frequency. Keywords: → ↑, fields

TABLE OF CONTENTS

Accesion For

NTIS CRA&I	☑
DTIC TAB	☐
Unannounced	☐
Justification	

By

Distribution /

Availability Codes

| Dist | Avail a..d / or Special |

A-1

iii

LIST OF ILLUSTRATIONS

LIST OF ILLUSTRATIONS (concluded)

v

SECTION 1

INTRODUCTION

As a result of the above-ground nuclear test ban treaty, DNA researchers have examined relevant non-nuclear structured environments as simulators of the late-time nuclear situation. Studies of these naturally-occurring environments are relevant because the convective instability processes that operate in high-altitude nuclear phenomena also occur naturally. Of the naturally-occurring disturbed environments, equatorial spread F is associated with the highest levels of structure--particularly at the peak of the solar cycle. Herein, we have analyzed the effects of such structure on the transionospheric propagation of radio signals from the DNA Wideband satellite.

Electron-density irregularities in the equatorial ionosphere provide considerable information about the processes responsible for their generation. Of particular interest to communications systems is the shape of the irregularity power spectrum over spatial scales between about 0.1 and 10 km. These irregularities have been measured in situ by satellite (AE-E, S3-4) and rockets (Plumex, Condor) as well as by remote means. The spectra from in situ measurements are relatively sparse, however, compared with a much more readily available measurement of the structure: complex signal scintillation. Phase scintillation measured over transionospheric paths at very-high through microwave frequencies provides a nearly direct measure of integrated irregularity structure, at least at weak disturbance levels.[1*]

During the operation of the DNA Wideband satellite, hundreds of passes of equatorial phase scintillation were obtained at Ancon, Peru, and Kwajalein, Marshall Islands. The phase spectral measurements made using

---

*References are listed in order of appearance at the end of this report.

1

these data provided much of the basis for DNA phenomenology modelling of irregularity spectral shape. In order to refine that spectral model, a selected portion of the Wideband equatorial data were recently reprocessed, using the techniques developed for the HILAT experiment. The purpose of the study was to obtain a characterization of the phase spectrum under weak and strong scattering conditions. Varying conditions result in spectral forms that are very different. In weak scatter, the phase spectrum reflects the in situ structure while the strong scatter spectral shape is significantly altered by diffraction.

The first portion of this report is concerned with weak scatter data only. DNA has recently accepted a two-component irregularity model, and SRI has obtained representative values of the slopes and break frequency for that model from the phase data. Fresnel nulls occur in most of the weak scatter phase spectra; the spectral fitting must carefully avoid that superimposed structure. In Section 2, we outline the approach we have used in the analysis, and present the observed phase spectral characteristics.

In our strong scatter analysis presented in Section 3, we have pursued two aspects of the effects of diffraction on phase. The first is the alteration of the temporal phase record during strong scattering; from this, an estimate of phase error as a function of intensity disturbance has been obtained. The second aspect is the overall shape of the phase error as a function of disturbance level; from this, some broad conclusions about strong scatter Fresnel effects on phase can be drawn.

2

SECTION 2

WEAK SCATTER ANALYSIS

2.1 ANALYSIS RATIONALE.

A major concern of those using phase spectra to imply irregularity structure is that the particular manifestations of diffraction on the phase spectrum are unknown. By diffraction, we mean any departure from the nominal linear dependence of signal phase on carrier frequency. Until the diffraction effects can be specifically identified, any conclusions regarding phase spectral shape should be based on weak scatter data only. A convenient range of disturbance level to work with which satisfies this criterion, is an intensity scintillation level of $0.2 < S_4 < 0.5$. The lower limit is necessary to avoid bias of the results caused by noise contamination. The upper limit follows from analysis (which is presented in Section 3); above this level of S_4, phase errors begin to rapidly increase and the phase spectral shape begins to be distorted. For the passes we have selected, virtually all of the equatorial Wideband data that fall into this weak scatter disturbance range are at 413 MHz and 1239 MHz.

Limiting the weak scatter analysis to low values of S_4 is not without its complications. In particular, Fresnel null structure is superimposed on most of the weak scatter phase spectra we observe. At 413 MHz, the weak scatter often arises from bottomside spread-F irregularities which are contained in relatively narrow and homogeneous layers below the F-layer peak. For Fresnel structure to occur in the phase spectra, the irregularity layer must fit the thin screen definition. Bottomside spread F approximates a thin screen, and Fresnel nulls should be conspicuous. At 1239 MHz, the irregularities producing weak scatter scintillations are much stronger. At the local time sampled by the Wideband satellite, they are often the decaying remnants of plume structures, which are less con-

3

fined in altitude and less homogeneous than bottomside structure. Thus, we expect Fresnel nulls to be less conspicuous at 1239 MHz than at 413 MHz, and this is the case.

Figure 1 shows an example sequence of simultaneous 413 MHz and 1239 MHz intensity and phase spectra showing Fresnel effects. (Note that these 1239 MHz spectra are not included in our weak scatter results because their S_4 levels were less than 0.2.) The arrows indicate the expected frequency of occurrence of the first Fresnel intensity peak and phase null, for the given pass geometry, an assumed irregularity anisotropy of 50:1 and a layer height of 350 km. The nulls are conspicuous, even in these spectra that have been smoothed for display, and persist even up to S_4 levels of ~ 0.7 at 413 MHz.

Unfortunately, the Fresnel nulls are so prevalent in the 413 MHz data that they complicate the extraction of spectral slope and break frequency information. This became clear when a multicomponent fit algorithm, used early in the processing, gave break frequency distributions that were dependent upon carrier frequency. This tendency contradicts weak scatter theory assumption that a break in the irregularity spectrum should appear in the phase spectrum at the same temporal frequency, independent of the carrier. Subsequent numerical simulations using the multicomponent fit algorithms verified that the carrier-dependent break distributions were, in fact, due to the Fresnel nulls.

To avoid such Fresnel null biases, we chose to obtain two linear fits over temporal frequency ranges near the low and high frequency ends of the phase spectrum. In selecting fit ranges, temporal frequencies affected by the primary Fresnel null at 413 MHz and 1239 MHz were avoided. For an F-layer altitude of 350 km and an irregularity anisotropy of 50:1, the 413 MHz primary null is centered somewhere between 0.7 Hz and 1.3 Hz, depending on propagation geometry. For 1239 MHz, the range is between 1.2 Hz and 2.2 Hz. Thus, the 413 MHz nulls limit the fit range for a low frequency segment, while those at 1239 MHz limit the useable high frequency fit range. Taking into account the width of the null, convenient fit ranges are 0.10 Hz to 0.56 Hz (-1.00 to -0.25 log Hz, approximately 4500 m
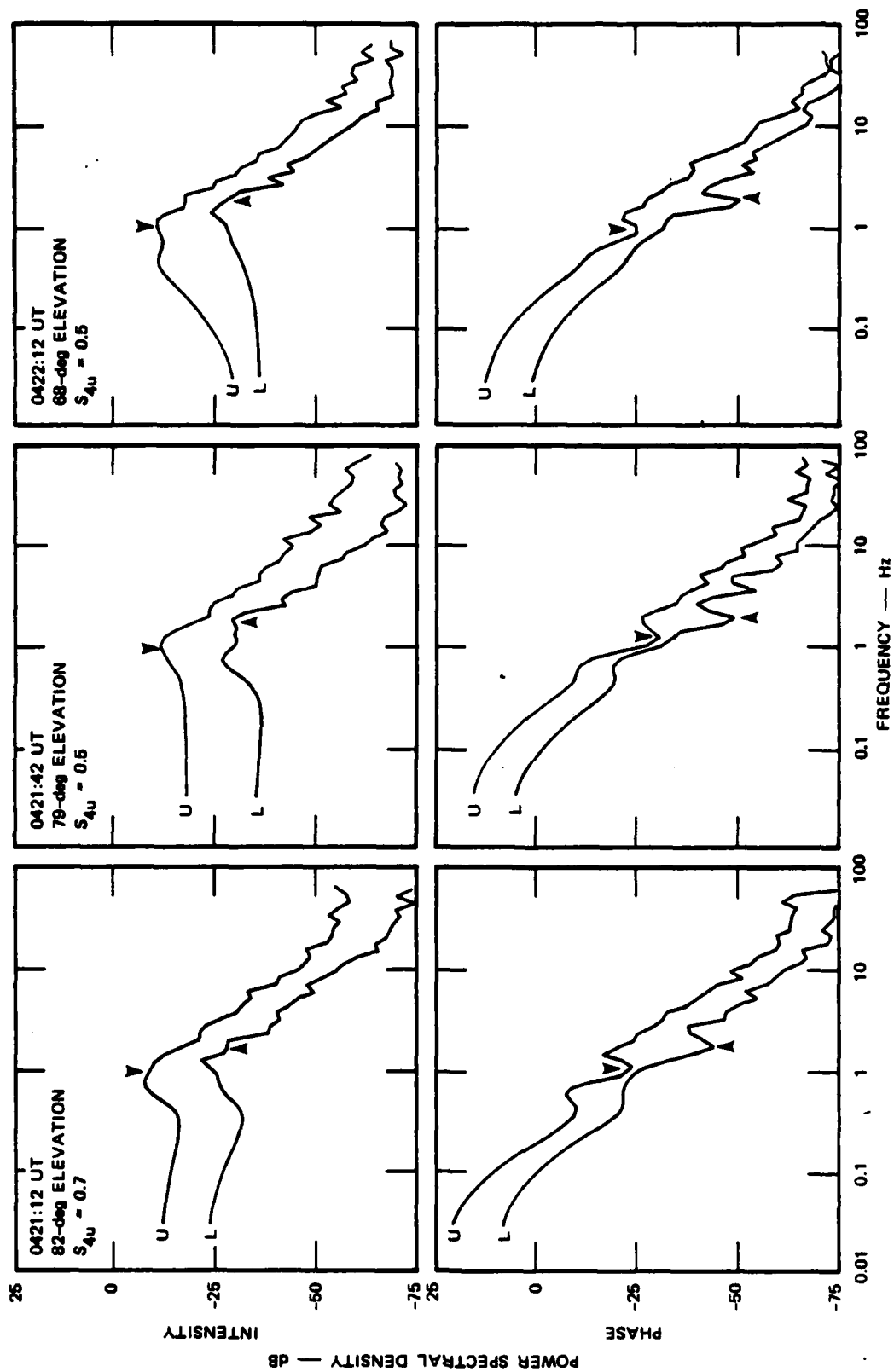
4

Figure 1. Intensity and phase spectra for 413 MHz (U) and 1239 MHz (L) from Ancon Wideband pass, Day 63, 1977, showing Fresnel effects. The relative Fresnel scale locations are noted with arrows.

5

to 800 m spatial scale), and 1.8 Hz to 10.0 Hz (0.25 to 1.00 Hz, approximately 250 m to 45 m spatial scale).

The outside range limits of 0.1 and 10.0 Hz were chosen primarily to maintain historical continuity with earlier Wideband analyses.[2] In addition, however, they avoid any possible low frequency spectral contamination caused by windowing, and high frequency contamination caused by system noise. Furthermore, if the power spectral density at 10 Hz was less than -50 dB rad^2/Hz (a conservative estimate of the Wideband system noise floor), the high frequency fit limit was chosen to end at that frequency.

We have also been careful to avoid contamination of the results by interference or by other spurious effects. This was done by applying relatively stringent requirements to each set of simultaneous 137 MHz, 413 MHz and 1239 MHz spectra. Any spectrum that was accepted had an integrated energy, which was consistent with that at the other two frequencies. More specifically, if the ratio between the rms phase deviations at two adjacent carriers exceeded 30 percent of the linear ratio, the spectra were rejected from the data base.

As for the spectral analysis, per se, we have used (up through the spectral slope fitting) the current HILAT in-field processing. This includes edge-matching and cosine-windowing of 30-s spans of data at 125 Hz before spectral analysis. Prior to obtaining the slopes, the phase power spectrum is log-decimated to 50.

For the reanalysis of the Wideband equatorial data, we chose 24 orbits from Ancon and 19 from Kwajalein. All were selected because they show consistent scintillation throughout most of each pass, i.e., at a variety of propagation geometries. The Ancon data are from the period February through April 1977; the Kwajalein data are from July through September 1977. These are the peak scintillation seasons at each longitude[3] in the year of maximum solar activity sampled by Wideband. The spectral parameter statistics from the two stations are virtually identical; what we discuss in the paragraphs below is a combined result.

6

2.2 POWER-LAW AND TWO-COMPONENT POPULATIONS.

Our primary interest is with two-component phase spectra for which the low frequency slope, P_a, is shallower than the high frequency slope, P_b. This spectral form does, in fact, comprise the majority of our observed spectra. There is also a population of spectra for which the two slopes, P_a and P_b, are very close to one another; as a practical matter, these are single power-law in form. The third category of spectra are those for which P_a is significantly steeper than P_b. Although approximately 30 percent of the spectra are of this form, we have discarded them from the statistics. Our justification is that this spectral form is almost never observed in situ at the equator. Most likely, the phase spectra of this type are a result of integration through multiple layers having different characteristics.

The working data set consists, then, of the two-component spectra with $P_a < P_b$, and the $P_a \sim P_b$ single power-law cases. Spectra are identified as single power-law if P_a is within 20 percent of P_b. This criterion is somewhat arbitrary; the specific percentage chosen does affect the single/dual power-law population mix, but does not significantly alter the slope or spectral break distributions. Using this criterion, the percentage of single power-law spectra is 37 at 413 MHz, and 28 at 1239 MHz. These percentages are not a strong function of carrier frequency, suggesting that the same irregularity process or mix of processes is operating over a wide range of turbulence strength. For example, the two-component spectra do not appear to be limited to the strong turbulence that produces 1239 MHz scintillation.

2.3 SPECTRAL SLOPES.

The distributions of the low- and high-frequency slopes, P_a and P_b, are shown in Figure 2 for the combined Ancon and Kwajalein spectra (excluding those for which P_a is much steeper than P_b, as noted above). The data for 413 MHz and 1239 MHz are shown. The weak scatter population at 137 MHz is too small to provide useful distributions, although the 137 MHz mean values of P_a and P_b are similar to those at the higher frequencies.
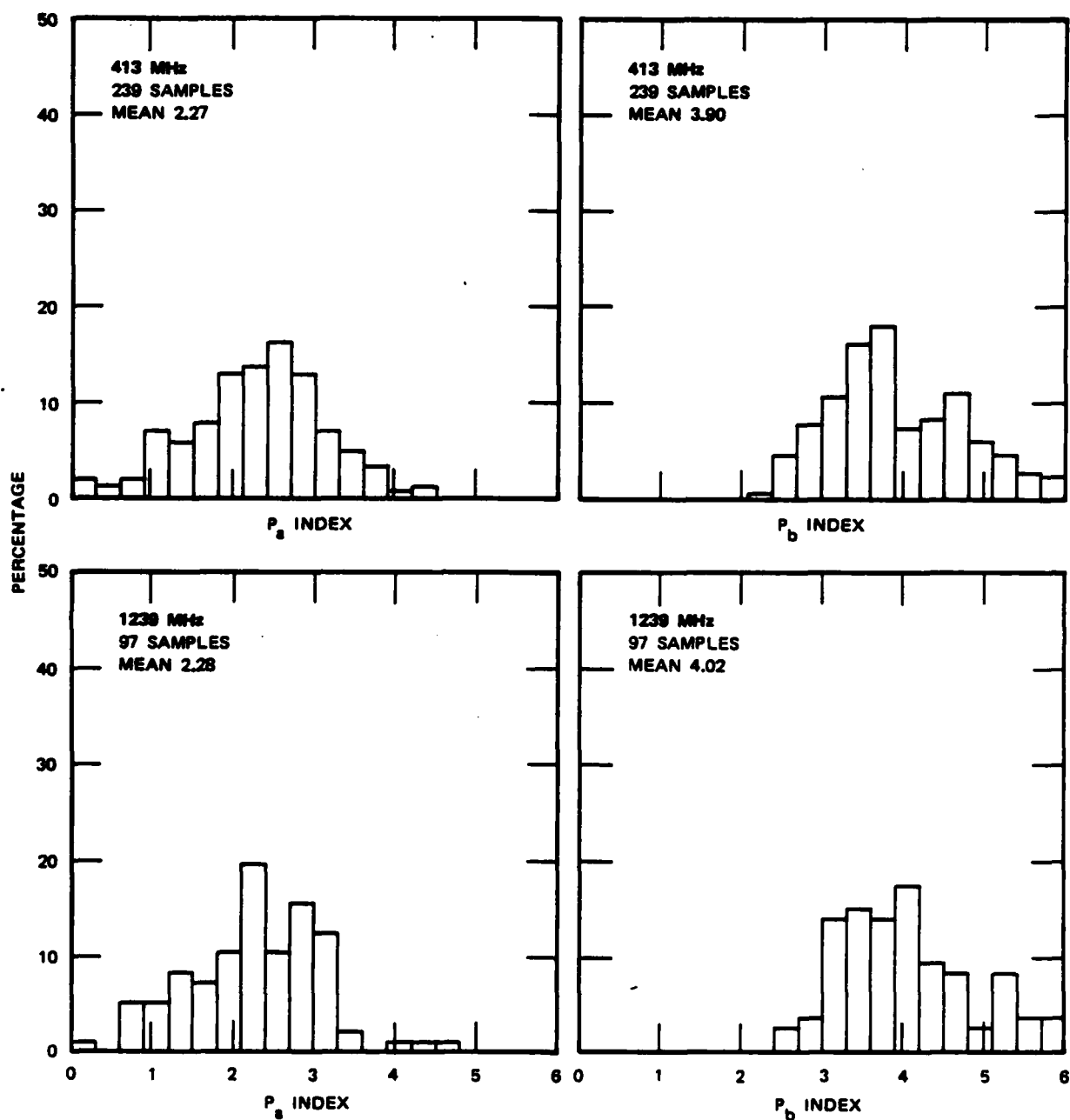
7

Figure 2. Distributions of the P_a and P_b phase spectral indices for 413- and 1239-MHz weak scatter.

8

The sample populations and the mean value for each distribution are noted. The shapes of the distributions for P_a and P_b are similar for the two carrier frequencies, and their means are nearly the same, with $P_a \sim 2.3$ and $P_b \sim 3.9$.

The agreement between the two carriers is an important result because it shows that (in weak scatter, at least) there is no appreciable shallowing of the spectral slope of either component with disturbance level. As mentioned previously, the irregularity structure that produces weak scatter scintillation at 1239 MHz is several times stronger than that causing the same signal disturbance at 413 MHz. Previous studies[2,3] and implications strong scatter temporal statistics[5] showed a shallowing of slope with increasing disturbance level. There should be explanations for this apparent discrepancy. In the case of Reference 2, the difference is caused by diffraction effects, as the data in Section 3 will show.

2.4 SPECTRAL BREAK SCALES.

In addition to the slopes, the spatial scale at which the two-component spectrum breaks is an important factor in characterizing the irregularity generation process. For phenomenological purposes, the spatial size at which this break occurs is termed the freezing scale. In the propagation case, a break in the irregularity spectrum appears in the phase spectrum at a temporal frequency dictated by the line-of-sight scan velocity. This, in turn, depends upon the irregularity altitude, anisotropy, and motion. The temporal frequency at which the translated break occurs is independent of carrier frequency, as previously noted. This lends credence to the interpretation that its origin is in situ.

The orbital inclination of the Wideband satellite is such that for the premidnight pass data used here, the propagation path scans nearly along the magnetic meridian. For F-region irregularities that are highly extended along the magnetic field (50:1 anisotropy), the effective scan velocity caused by the satellite motion has an average value of ~ 0.45 km/s. At the local time and latitude of the observations, F-region polarization and tidal electric fields will typically drive the irregu-

larities eastward at a velocity of ~ 0.25 km/s. The total effective scan
velocity will then be in the 0.5 km/s to 0.7 km/s range.

For each spectrum, the break frequency is taken to be at the inter-
section of the P_a and P_b linear fit segments. The distribution of the
break frequencies is shown in Figure 3 for 413 MHz and 1239 MHz. The
distributions for both carriers are broad, and are similar in shape and
mean value. Much of the broadening of the distribution is because the
scan velocity of the propagation path through the irregularities depends
upon the propagation geometry. A break at a fixed spatial scale will
therefore appear at different temporal frequencies throughout the course
of a pass. If there were a means of accurately applying correction for
the scan velocity so that the data could be sorted in spatial scale, the
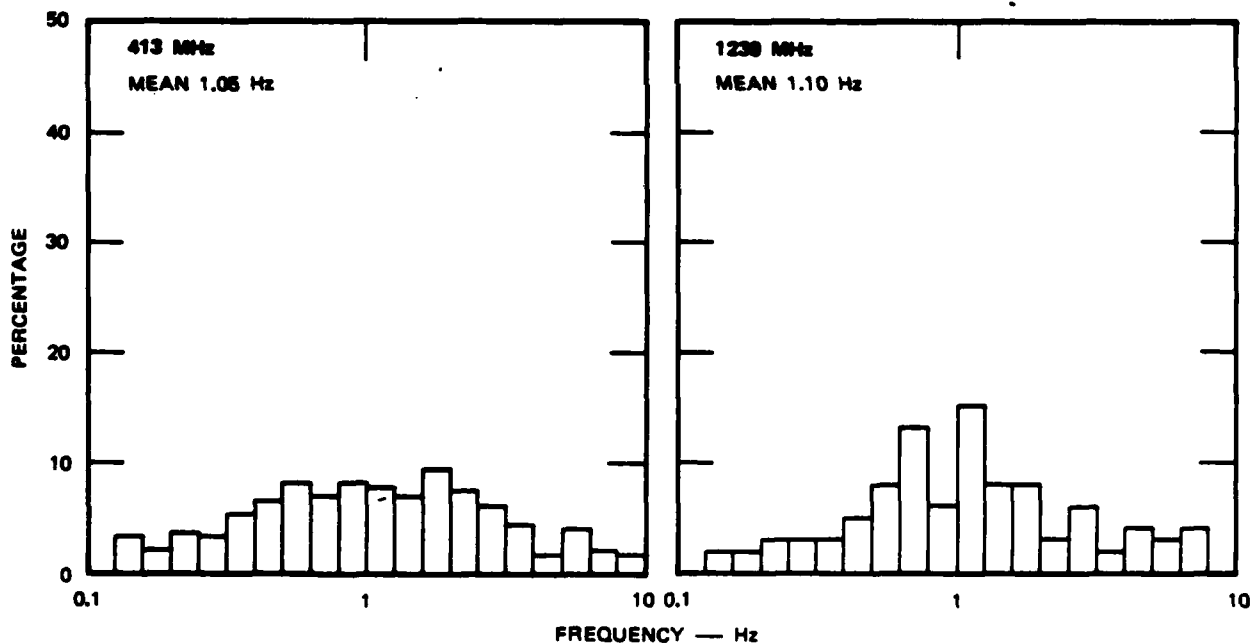distributions would be much narrower.

Figure 3.   Distributions of phase spectral break frequencies.

10

Choosing an overall average break frequency of 1.07 Hz, and a representative scan velocity of 0.60 km/s, our estimate of the irregularity break scale is near 0.65 km. This is in good agreement with the irregularity spectrum break scale observed by satellite and rockets—typically reported as 0.75 km. The difference is probably not significant, because the phase-implied value is highly dependent upon our scan velocity assumptions about layer height and irregularity anisotropy.

2.3 COMPARISON WITH PREVIOUS STUDIES.

It is worthwhile to compare the original Wideband slope results[1] with those obtained here. For the earlier Wideband analysis, the slopes were extracted between 0.1 Hz and 10.0 Hz (as has been done here), but it was presumed that the spectra were of single power-law form. There were additional differences, however, in the pre-fit processing, which could have had an effect on the spectral index statistics. These were: (1) prior to spectral analysis, the temporal records were filter detrended but not windowed, and (2) no requirements were placed on rms phase deviation ratios, nor were precautions taken to avoid noise contamination of the fits at low disturbance levels.

To determine whether the current pre-fit reprocessing (windowing and stringent sorting) has significantly affected the slope statistics, we have made single power-law fits (0.1 Hz to 10.0 Hz) for our reprocessed passes. The results are shown in Figure 4, adjacent to the replotted results.[1] We can see that the current analysis slopes are systematically steeper than those from the original analysis. For S_4 levels less than about 0.3, this is not unexpected because the Wideband spectral fit range included the noise floor [Item (2), first paragraph of this section]. Reference 1 noted this fact, and in our reanalysis, we have specifically avoided noise contamination.

For $S_4 > 0.3$, where noise is not a problem in the spectral fits, the revised slopes are also steeper than the original by about 5 to 10 percent. This is most likely an effect of sidelobe contamination of the high frequency portion of the original spectra. This is a common problem with

11
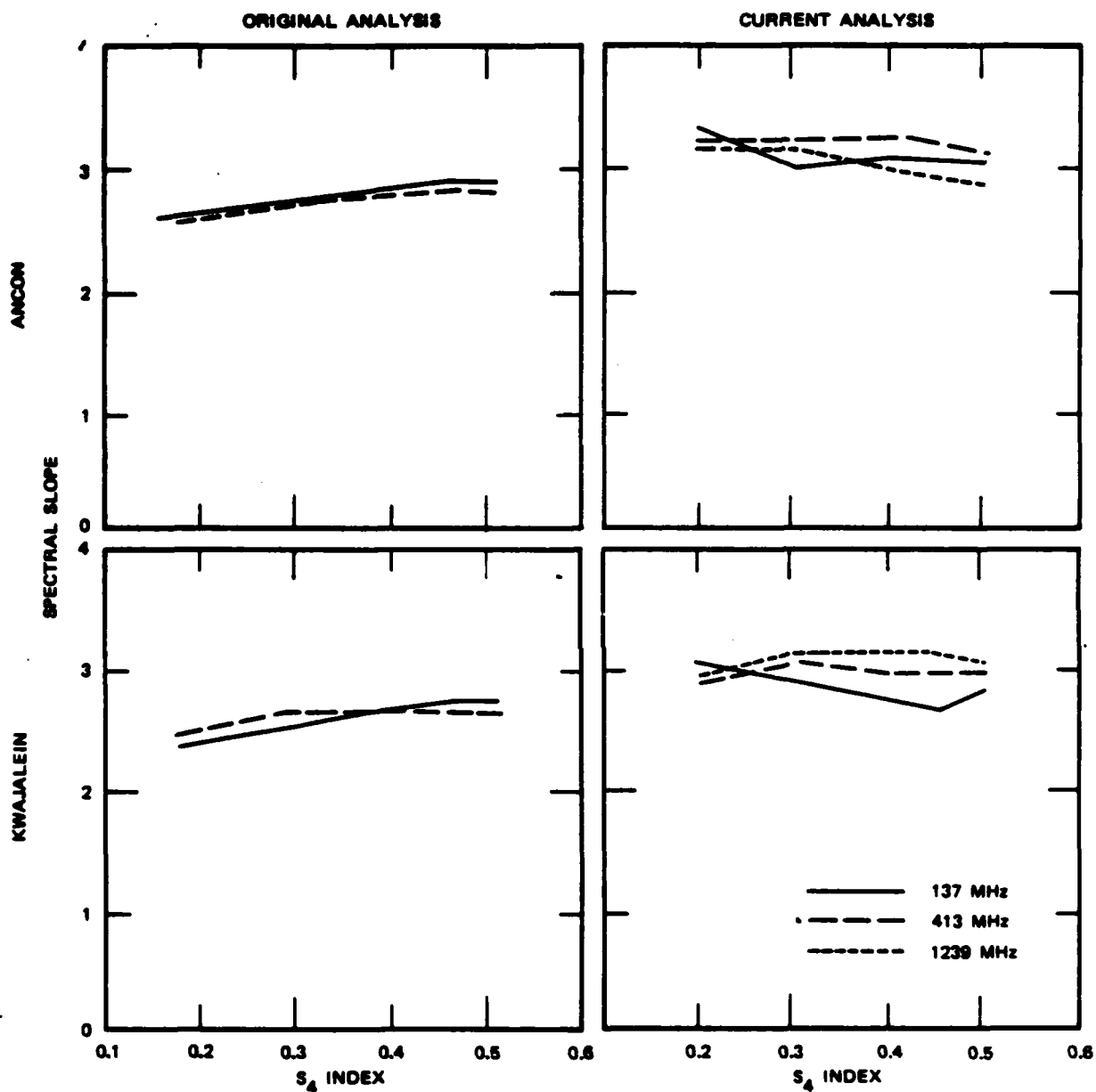
Figure 4. Comparison between original and reanalysis Wideband phase slopes assuming single power-law form.

12

spectral analysis of power-law processes; we now eliminate the sidelobes by windowing the temporal records.

The revised value of slope near 3.0 is undoubtedly a more accurate representation of the underlying irregularity spectrum than were the original Wideband values of ~ 2.5. The difference does point out, however, that there was a deficiency in the earlier Wideband processing, the difference is of little consequence. In terms of understanding irregularity processes, a much more important shortcoming of the original Wideband analysis was the presumption that the phase spectra were purely power-law.

SECTION 3

STRONG SCATTER ANALYSIS

The weak scatter phase spectral form remains consistent up through a disturbance level for which the S_4 index is approximately 0.5. Above this level, however, the shape of the phase spectrum is significantly and progressively altered by diffraction processes. As an example, Figure 5 shows this change of spectral shape in terms of the mean value of P_a and P_b indices at 137 MHz and 413 MHz during moderate to strong scatter. The slopes of both the low and high frequency portions of the spectra depart from the weak scatter values of $P_a \sim 2.3$ and $P_b \sim 3.9$ for $S_4 > 0.5$, and systematically become more shallow at stronger scatter levels.

We will consider two aspects of the behavior of phase scintillation under strong scatter conditions. The first is a look at the details of phase temporal behavior in strong scatter. This provides estimates of diffraction-induced phase errors and how they arise. We then give an overall view of the phase spectral shape as a function of scattering level, from which some broad conclusions regarding Fresnel dependence can be made.

3.1 TEMPORAL CHARACTER OF PHASE IN STRONG SCATTER.

The Wideband experiment provided a nearly ideal means to study the onset and development of diffraction effects on signal phase. This was the Wideband UHF comb, seven carriers transmitted by the spacecraft beacon at a spacing of approximately 11 MHz, between 378 MHz and 435 MHz. We have used these data to estimate the nature and degree of alteration of the phase temporal record by diffraction. The reasoning is that two UHF signals separated by only 11 MHz should undergo nearly identical propagation effects, while those separated at multiples of 11 MHz up through 66 MHz should exhibit increasingly different diffraction effects. It is thus
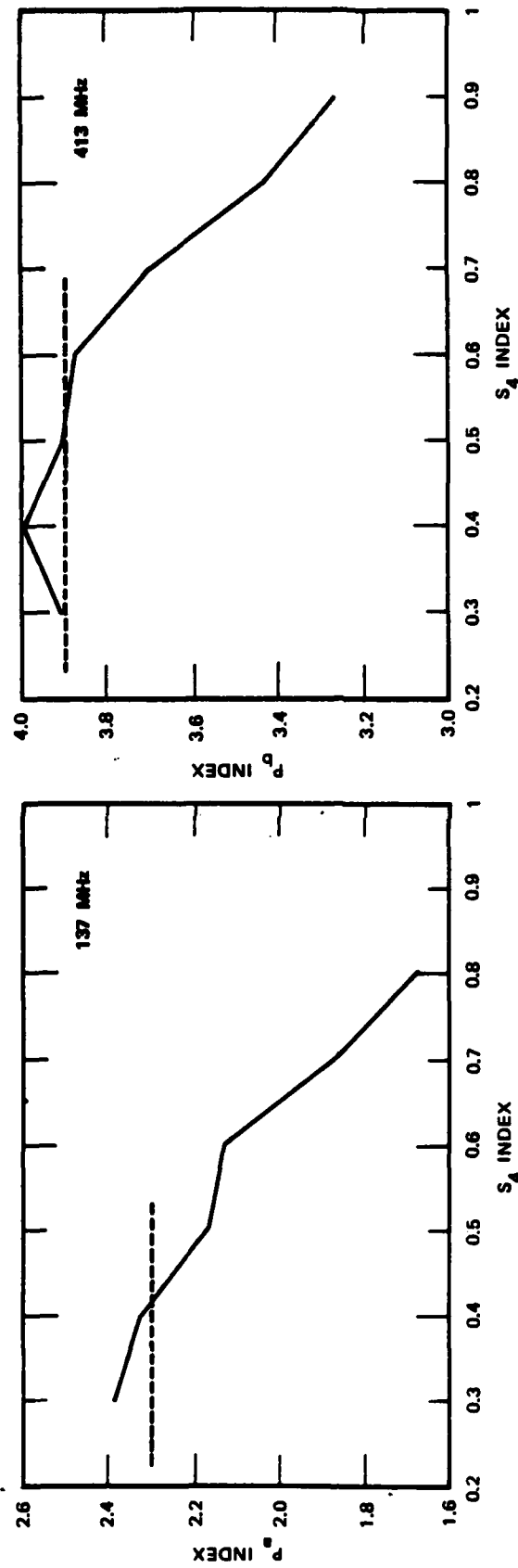
14

Figure 5. Phase spectral shape behavior in strong scatter, as characterized by the P_a and P_b spectral index dependence on S_4. The dashed lines indicate the values found from the weak scatter analysis.

15

possible to observe diffraction-induced detail in the signal structure, which would not be possible in a comparison between more widely spaced carriers.

For the analysis, we chose a high-elevation Wideband pass from Ancon, for which the UHF scintillation ranged from weak to saturated. The first-order statistics (S_4 indices and rms phase deviations) for the 137 MHz and 413 MHz Wideband carriers are shown in Figure 6. As can be seen, the scintillation change is relatively systematic over the duration of the pass and shows no particular dependence on propagation geometry.

Figure 7 shows the signal intensity and phase records for one 30-s portion of the pass, comparing the 413 MHz and 378 MHz carriers. The phase data have been edge-matched and windowed, i.e., as prepared for routine spectral analysis. Also shown is the difference between the phase records at the two carriers, following the slight but necessary linear scaling for measurement frequency.

For this particular span in the figure, the scintillation is moderate ($S_4 \sim 0.6$), and even though the carriers are separated by 33 MHz, the phase records are virtually indistinguishable. This is confirmed by the phase difference plot, which is near zero, although a series of small and rapid excursions can be seen. These are caused by cusp-like changes in phase, which occur in the signal minima of intensity fades. In this case, where the fades are only a few decibels, the cusps have deviations that are only a few degrees from the nominal phase record.

Figure 8 shows a second 30-s span, where $S_4 \sim 0.75$. Diffraction has produced quite different intensity records at the two carriers, and the corresponding phase cusps are large enough to significantly alter the phase record. The two records are similar only in their large-scale variation; their difference is step-like, due to the large phase changes that occur during fades at one or the other carrier.

Finally, Figure 9 is a third 30-s span for near-saturated scintillation ($S_4 \sim 0.9$). The near-continuous fading of both carriers produces

16
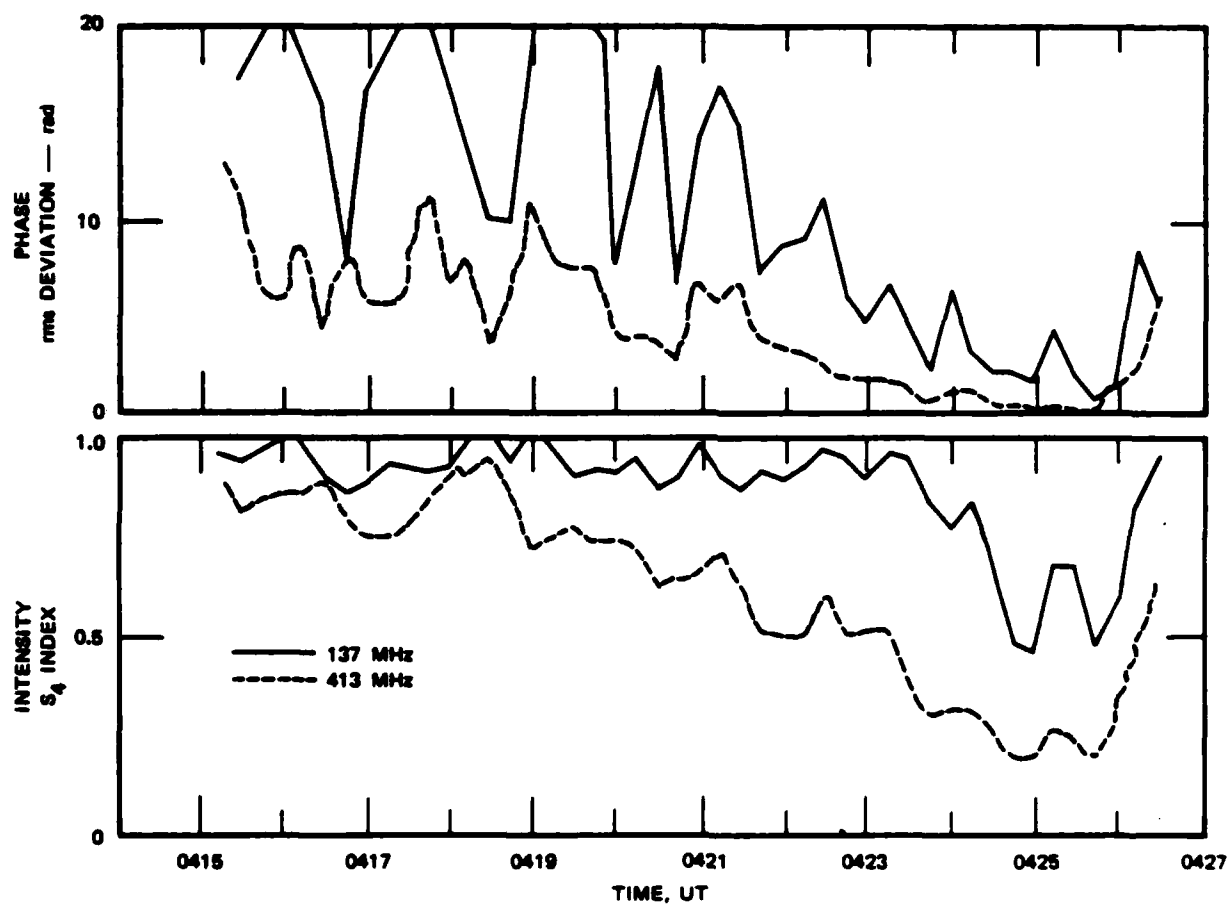
Figure 6.   First-order statistics for Ancon Wideband pass, Day 63, 1977.
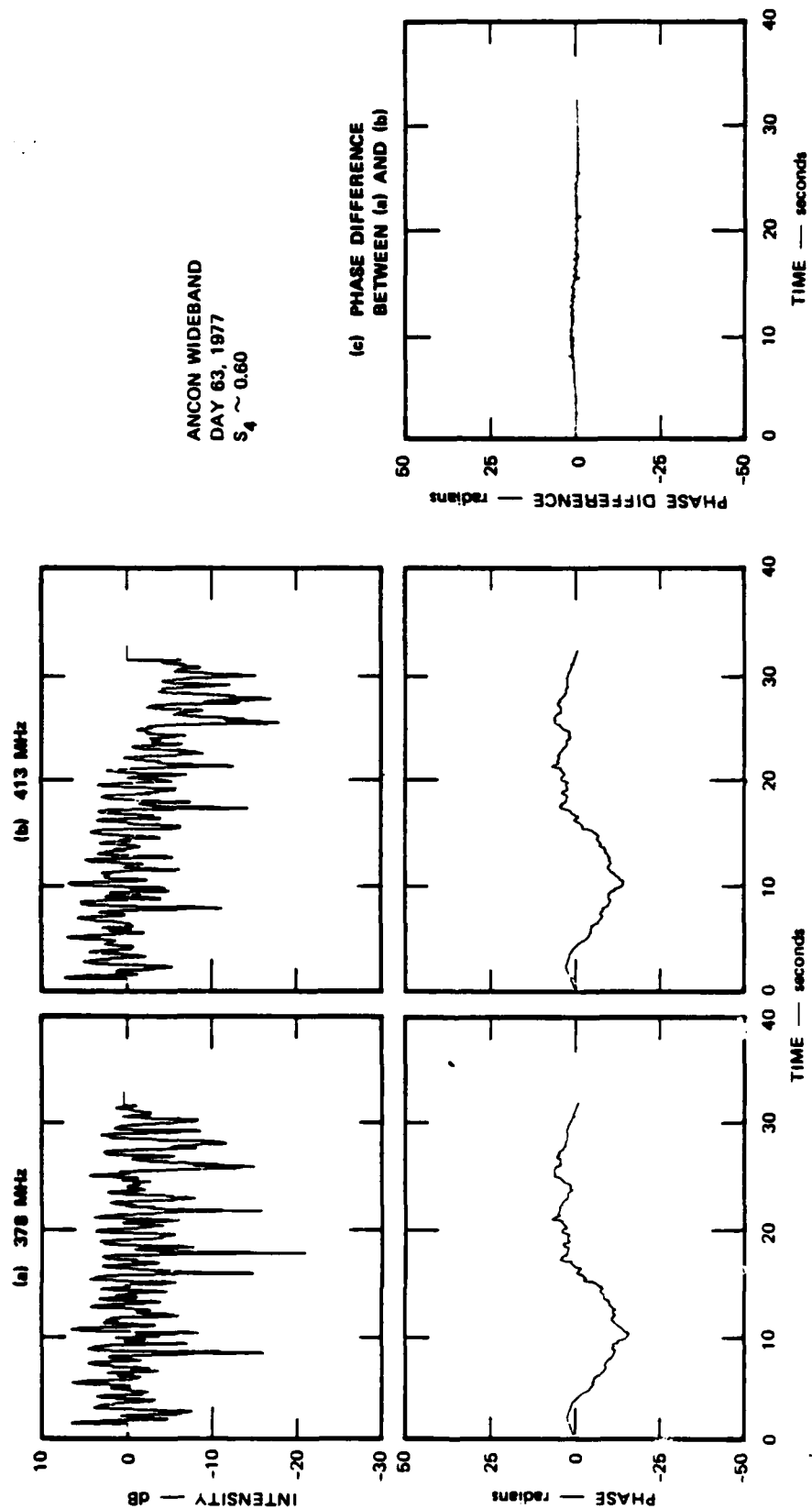
Figure 7. Comparison between simultaneous 30-s spans of Wideband data ($S_4 \sim 0.60$).

18
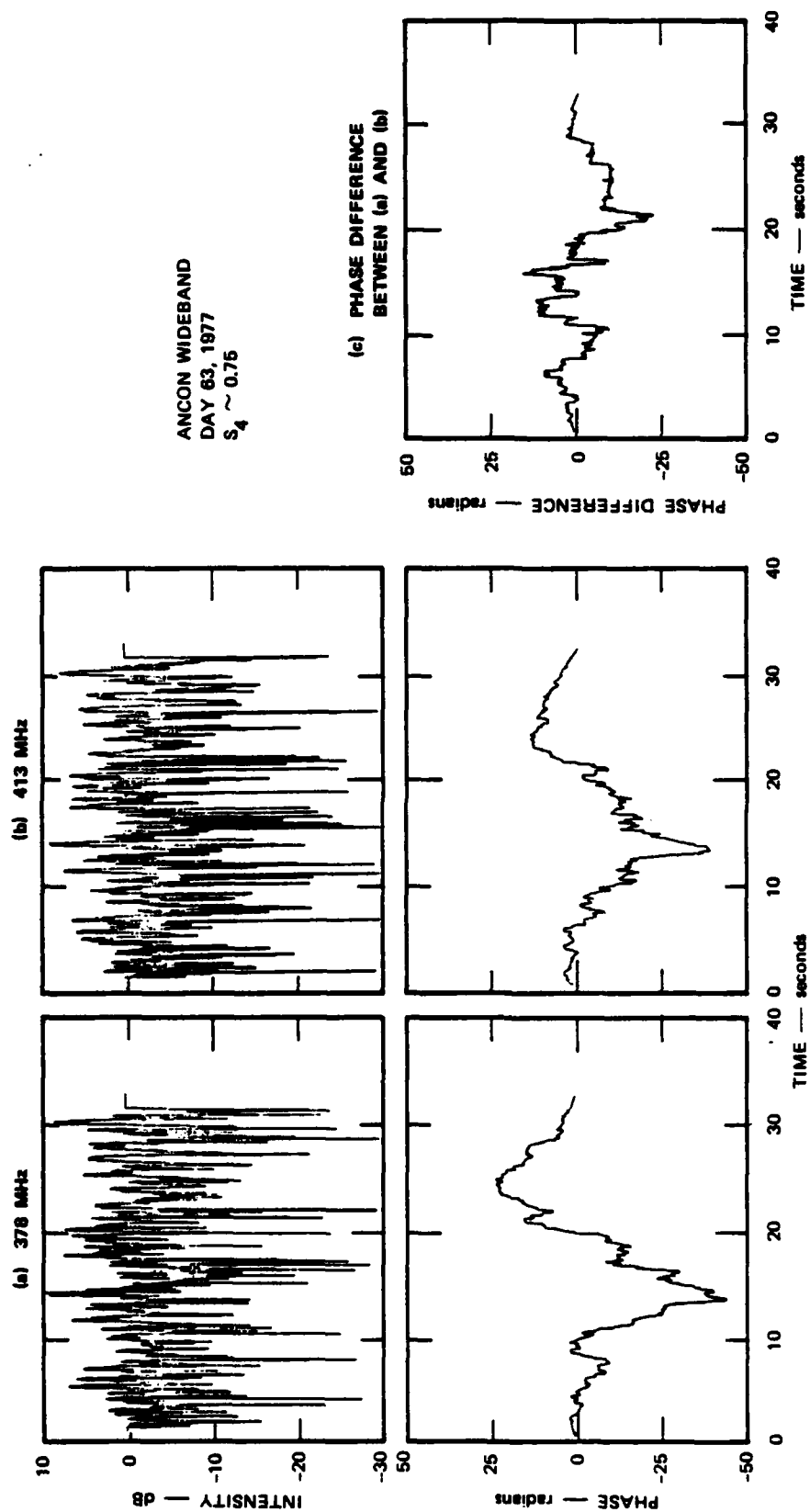
Figure 8. Comparison between simultaneous 30-s spans of Wideband data ($S_4 \sim 0.75$).

ANCON WIDEBAND
DAY 63, 1977
$S_4 \sim 0.75$

(c) PHASE DIFFERENCE
BETWEEN (a) AND (b)

(a) 378 MHz

(b) 413 MHz

19

ANCON WIDEBAND
DAY 63, 1977
$S_4 \sim 0.90$

(c) PHASE DIFFERENCE
BETWEEN (a) AND (b)

Figure 9. Comparison between simultaneous 30-s spans of Wideband data ($S_4 \sim 0.90$).

20

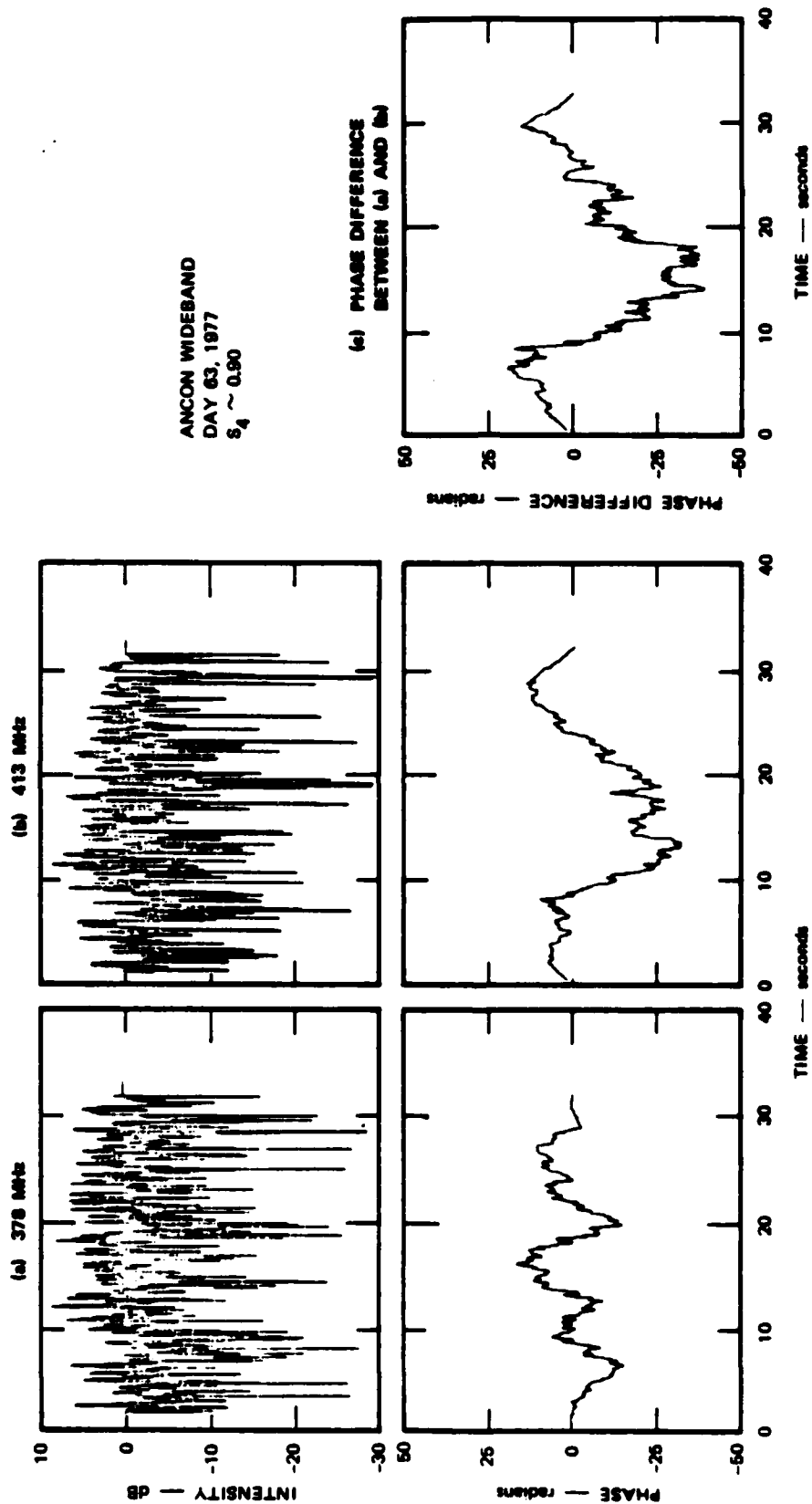phase records that are not even similar, thus the phase difference is more random and has lost the step-like character of the previous figure.

From these examples, it can be seen that phase cusps during fades are the primary source of diffraction contamination in the phase spectra for moderate through strong scatter. A key point is that the cusps in each phase record depend upon the details of the diffraction-generated signal intensity structure, and those details change very rapidly with measurement frequency. As a result, even for closely spaced carriers, minor differences in the characteristics of the two fading signals can result in reconstruction of very different temporal phase records. We point out that intensity correlation between carriers, per the conventional definition[5] reflects very little of the intensity structure detail that controls the phase cusps; for example, the intensity records in Figure 9 are correlated above 80 percent.

It is also useful to note that the phase cusp behavior during fades is not dependent (to first order) upon data sampling rate. The phase data in Figures 7 through 9 were constructed from quadrature components using a sampling rate of 125 Hz. We have repeated the process using the full Wideband sampling rate of 500 Hz, and have obtained records nearly identical to those from the lower reconstruction rate. To see no change despite a four-fold increase in temporal resolution shows that the phase cusps are adequately sampled, and are not caused by a failure to keep track of rapidly changing phase during a fade.

In Figure 10, the standard deviation of the diffraction-induced phase differences are plotted as a function of S_4. Each point corresponds to 30-s spans such as those shown in Figures 7 through 9. Three carrier separations are shown, 66 MHz, 33 MHz, and 11 MHz; the 66 MHz spacing data are from the outside carrier pair of the UHF comb (435 MHz and 378 MHz); the 33 MHz and 11 MHz spacing data are from various carrier pair combinations within the comb. A least-squares quadratic fit has been made to each block of data to illustrate that the diffraction-induced phase difference dependence on S_4 index is nearly the same for all three carrier separations. We note that in weak scatter, the differences are small (~
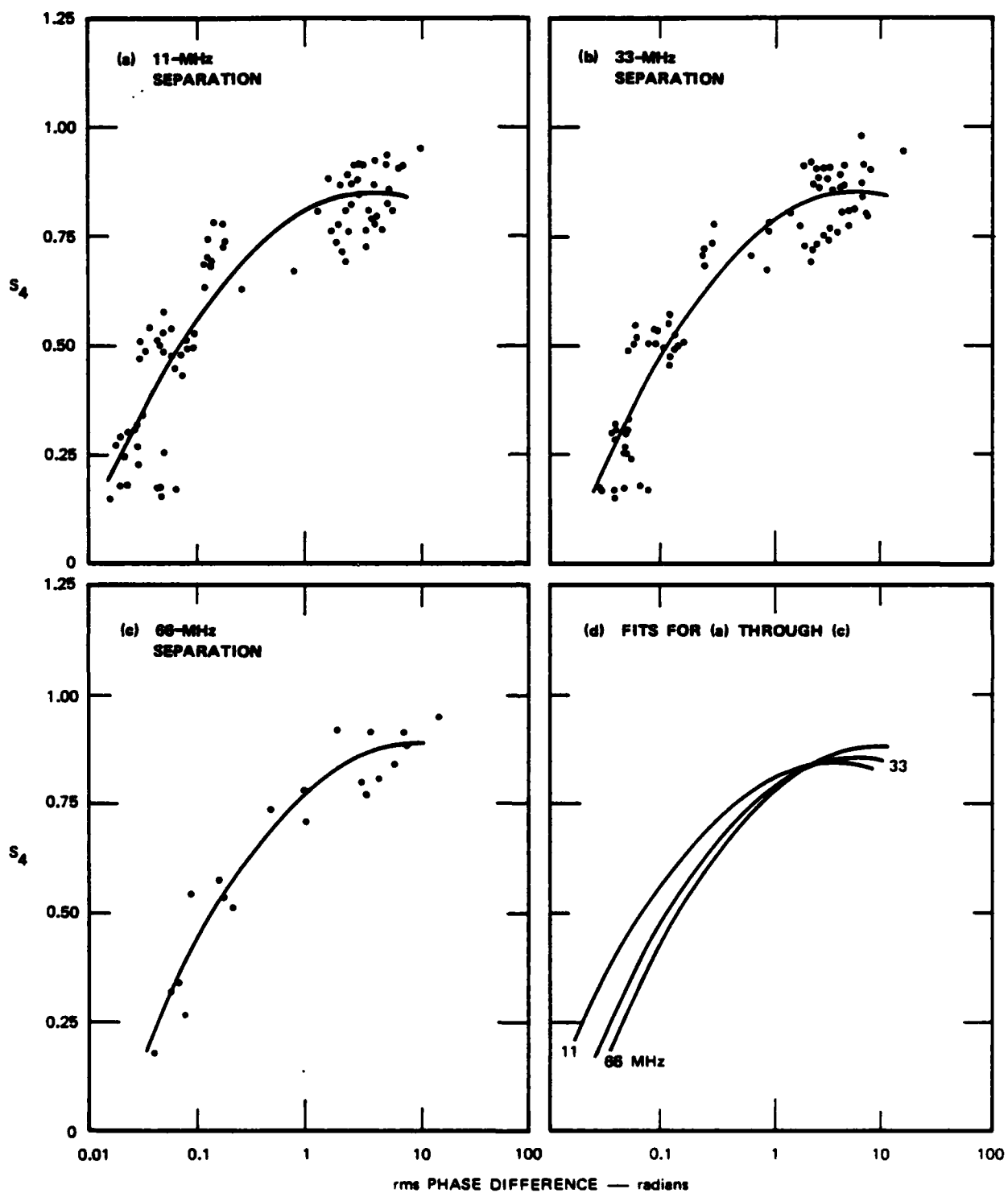
21

Figure 10. Standard deviation of diffraction-induced phase differences using Wideband UHF comb carriers.

20 deg), even for the 66 MHz spacing; this is most likely not due to phase cusps. It is apparently a result of differential Fresnel null structure. In addition, there is dispersion in the spacecraft antenna, which produces the weak large-scale trend that can be seen in Figure 7.

The dependence of the diffraction-induced phase errors on carrier separation are shown more clearly in Figure 10(d), where the least-squares fits are compared. As the level of disturbance increases from weak scatter to $S_4 \sim 0.6$, the separation of the curves remains nearly constant. The curves then begin to converge until at $S_4 \sim 0.8$, the phase differences become independent of carrier separation at a value near 8 rad.

The important point to be made from Figure 10 is that diffraction can create significant differences in phase structure even between closely spaced measurement frequencies. Thus, even at moderate scatter levels ($S_4 \sim 0.6$), there will be differences in phase spectral shapes measured at UHF carriers separated by only a few tens of megahertz. Again, this is because the phase structure depends almost entirely on the details of the diffraction-developed intensity structure.

It is possible to use the result in Figure 10 to estimate the diffraction contamination that would be encountered in the case of a single carrier measurement. First, we note that the rms phase differences in the figure include contamination from phase cusps at both carriers. As the carrier separation increases, so does the dissimilarity of the intensity fade patterns; thus, the total number of phase cusps from the two carriers increases. In this sense, the carrier separation dependence of the phase difference in Figure 10 is a product of (and is applicable only to) the closely spaced carrier measurement. In the case of the single carrier measurement, diffraction structure at any frequency would be no different from that at any one of the comb carriers for the same disturbance level. Yet, single carrier phase would be compared to a coherent reference phase from a carrier at least 1000 MHz away, and presumably undisturbed. Thus, the single carrier diffraction effect in phase should be comparable to or

23

less than those from our most closely spaced comb carriers, i.e., a few degrees at $S_4 \sim 0.5$ and a few radians at $S_4 \sim 0.9$.

This result is also in satisfactory agreement with the average spectral shape data shown in Figure 5. At $S_4 \sim 0.5$, where the integrated phase error due to diffraction is only a few degrees, there can be little spectral shape distortion, as is the case. On the other hand, when the scintillation is saturated, we expect, and see, significant distortion in both the high and low frequency portions of the phase spectrum as is consistent with an rms phase differences of a few radians.

3.2 PHASE AND INTENSITY SPECTRAL SHAPES IN STRONG SCATTER.

Knowing something of the manifestations of the diffraction process in the phase temporal records, we now turn to a brief review of how that structure is distributed in the phase spectrum, i.e., the spectral shape in strong scatter. Figure 5 provides a glimpse of the spectral shape dependence on disturbance levels in terms of P_a and P_b indices, which shallow at both low and high frequencies. In strong scatter, of course, characterization of the spectrum by P_a and P_b is probably inappropriate, because the spectral form may be altered or disguised by diffraction effects.

Strong scatter theories abound in the literature, and there are various approaches to the problem.[6,7,8,9.] By and large, these theories and numerical simulations address only the signal intensity behavior, and most are limited to gaussian or power-law source spectral shapes. There is generally good agreement between observation and predicted strong scatter intensity spectra. The shape of the intensity spectrum in strong scatter is dominated by the Fresnel scale for the particular propagation geometry and operating frequency, just as it is in weak scatter. As the perturbation level increases from weak through strong scatter, the narrow peak of the weak scatter intensity spectrum broadens toward both high and low frequencies. This bulge has the effect of shallowing the low frequency portion of the spectrum, but steepening the high frequency end, because the intensity structure at short spatial scales remains constant. Further-

24

more, between the Fresnel scale and the high frequency limit of the intensity structure, the spectrum is close to gaussian in shape, having continuous curvature. This means that because of the Fresnel scale dependence on carrier frequency, spectral slopes extracted from the same high frequency portion of intensity spectra will systematically depend upon that frequency.

Very little work has been done with strong scatter phase behavior, either observationally because of measurement difficulty, or theoretically because of inadequacies in the propagation models. The conventional opinion is that the phase spectrum should become more like the intensity spectrum as the scintillation level approaches saturation.[10] Presumably then, we should see a transition from the weak scatter two-component form to one with a broadening of energy centered on the Fresnel scale.

The reprocessed Wideband data affords an excellent opportunity to investigate strong scatter effects on the phase spectrum. However, because of the uncertainty about distortion of the spectral shape by diffraction, we have chosen not to extract spectral indices by curve fitting. Instead, the spectra have been sorted into S_4 ranges and averaged. This approach is not without its shortcomings; in particular, the average spectrum tends to be dominated by the most strongly disturbed spectra in each range. The essence of the spectral shape is not lost, however, as is shown in Figure 11, where the average phase and intensity spectra are shown for the weak scatter (S_4 range 0.3 to 0.5) at 413 MHz. Fits to this averaged phase spectrum over the selected frequency ranges for P_a and P_b give indices quite close to those in the slope distributions of Figure 6; P_a is 2.3, as was found from individual fits, while P_b is 3.7 compares well with the distribution value of 3.9. Thus, we feel that spectral forms obtained from averaging are accurate enough to be a useful means to characterize the complex signal behavior in strong scatter.

In passing, two additional points can be made from the weak scatter spectrum in Figure 11. First, even after averaging over a wide variety of propagation geometries, the spectrum still clearly shows the Fresnel null near 1 Hz; this is an indication of how prevalent that propagation feature
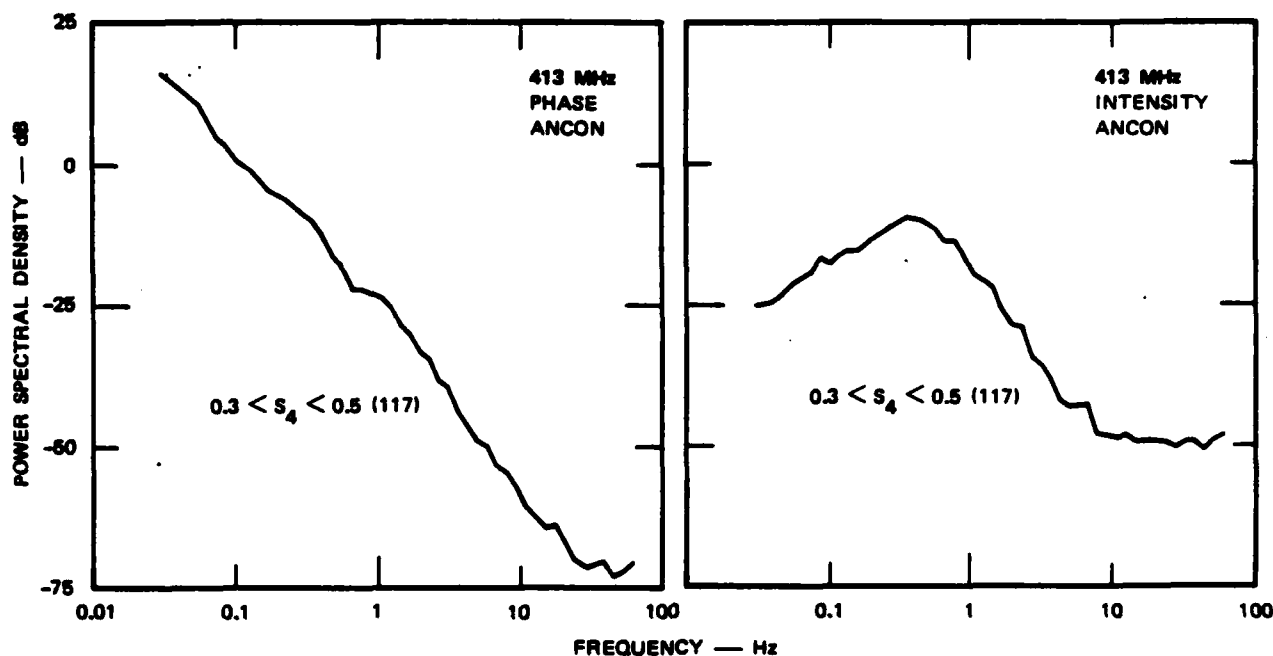
25

Figure 11. Average weak scatter spectral forms.

is in weak scatter spectra. A second point is that at first glance, the
spectrum appears to be of single power-law form--even though we know it is
a component spectrum having very different values of P_a and P_b. This
emphasizes the need for consistent and careful numerical (not visual)
curve fitting in comparative studies.

Figure 12 is a comparison sequence of weak through saturated scintil-
lation intensity and phase spectra at 413 MHz. The S_4 ranges and sample
populations for these average spectra are as indicated. For reference on
the phase spectra, the overall weak scatter P_a and P_b regimes are shown.
The intensity spectra in the figure generally exhibit the behavior predic-
ted by strong scatter theory. Starting from the weak scatter form, where
the intensity spectrum peaks at an average Fresnel scale, the spectra
broaden as the perturbation strength increases. As noted above, the
effect is a bulging of the spectrum from a point near the Fresnel scale to
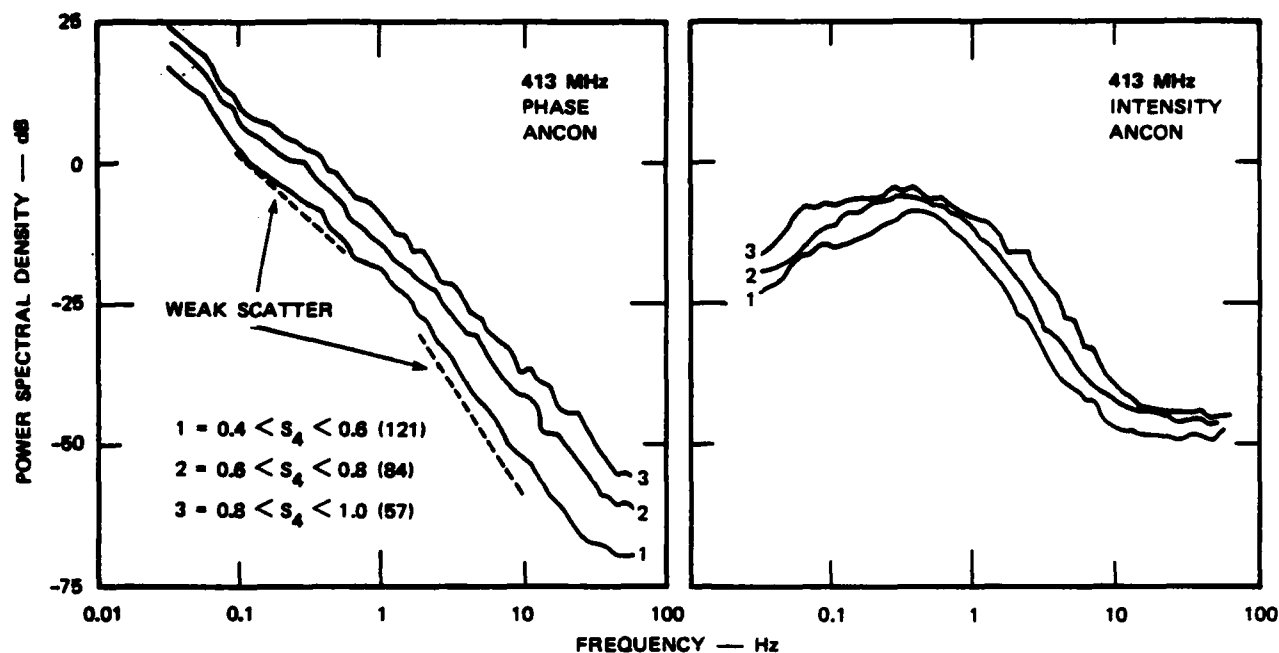both lower and higher frequencies.

26

Figure 12. Average strong scatter spectral forms as a function of disturbance level.

The corresponding changes in the phase spectra between weak and strong scatter are less conspicuous, except for a general upward shift as the phase variance increases. However, the shallowing of the overall spectrum indicated by Figure 5, can be seen. Figure 12 also shows that the increase in phase power spectral density is most rapid at higher temporal frequencies.

In order to look more closely at the change in spectral shape, and to see, in particular, if there are Fresnel dependences in phase, differential power spectral densities have been calculated for different S_4 values. These are shown in Figure 13 for 137 MHz and 413 MHz. The quantities shown are the differences between the phase power spectral density at the S_4 range indicated and those in the average spectrum for an S_4 range of 0.4 to 0.6. The intensity plots show how consistently the Fresnel scale dominates the intensity spectral shape. At the Fresnel scale, the power spectral density remains nearly constant, even into
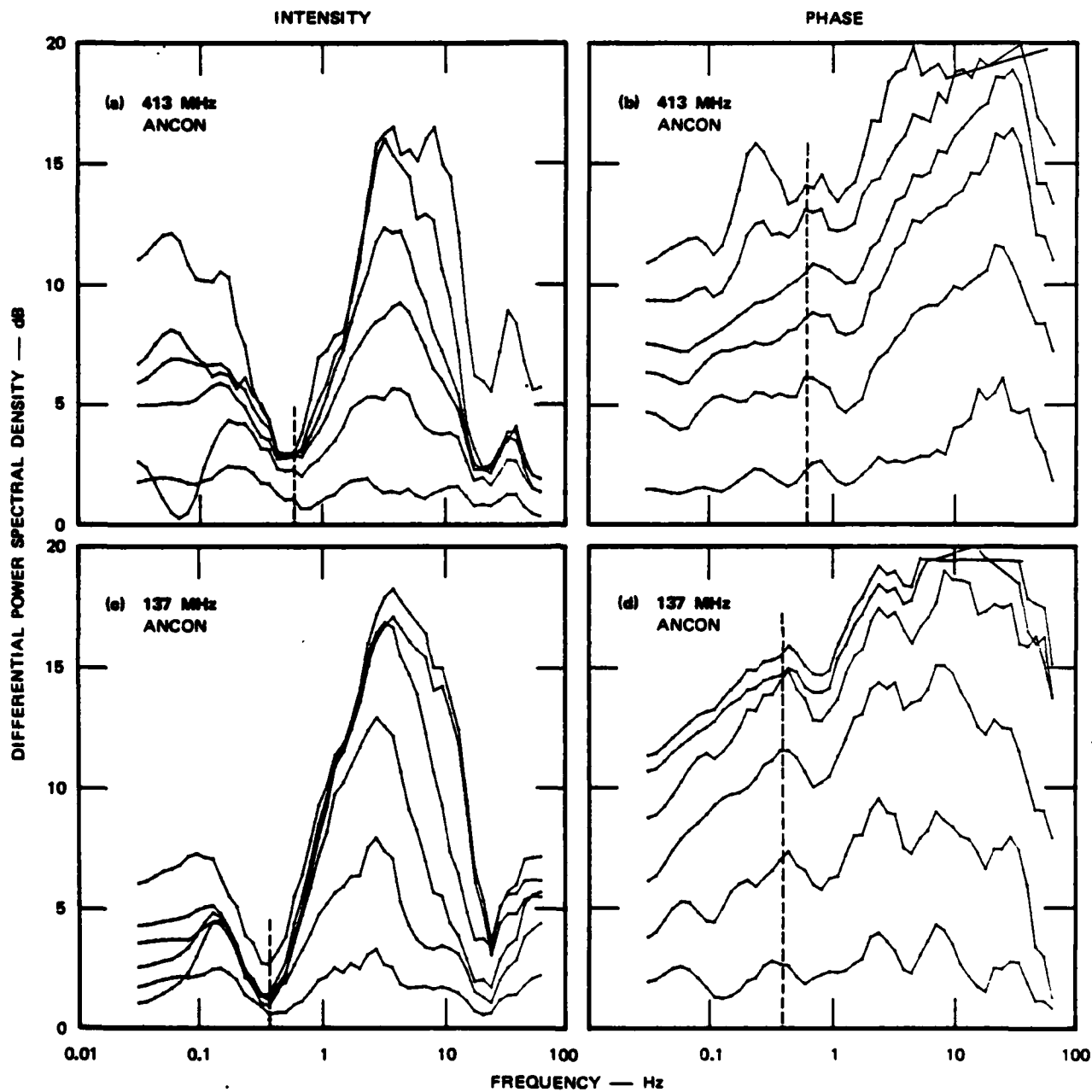
27

Figure 13. Differential power spectral density as a function of disturbance level, referenced to average power spectral density for $0.4 < S_4 < 0.6$. Relative Fresnel scales are indicated.

saturation. Lines indicate the expected relative locations of the 137 MHz and 413 MHz Fresnel scales, and they line up precisely with nulls in the differential spectral densities. The figure also shows that there is little change in the frequency at which the intensity spectrum changes slope, despite the large change in spectral energy.

The differential power spectral densities also show that the phase spectra in strong scatter have a less obvious but recognizable dependence on Fresnel scale. If we first consider the 413 MHz data [Figure 13(b)] there are two regimes in differential spectral density, separated by a peak-null pair near 1 Hz. The peak of this feature is aligned with the Fresnel scale, and is just the primary phase null that was our concern in the weak scatter analysis. At spatial scales larger than the Fresnel scale, the spectral energy gained with increasing disturbance is more uniform and less rapid than it is at shorter spatial scales.

At 137 MHz, the Fresnel null effect in the differential spectral density is also clear. What is less clear, relative to the 413 MHz data, is that there is a distinct demarcation between the rate of energy gain at spatial scales above and below the Fresnel scale. If the scale size dependence, which is so clear in the 413 MHz data, is purely a propagation effect, it should be observed at 137 MHz.

We speculate that the difference in scale size dependence between the differential power spectral densities at 137 MHz and 413 MHz is a result of Fresnel effects acting on a two-component irregularity spectrum. The nominal freezing scale in the two-component spectrum is near 750 m, which is very near the 413 MHz Fresnel scale for the average Wideband propagation geometry. At 137 MHz, the corresponding Fresnel scale is near 1300 m. In the case where the Fresnel and freezing scales are aligned, the strong scatter spectrum could reflect and even accentuate the underlying two-component nature of the source spectrum. Simulations[9] have shown that the strong scatter intensity spectrum depends critically on the slope of the source spectrum in the vicinity of the Fresnel scale; this may be even more the case with phase.

29

A more detailed analysis of the dependencies of the phase spectra is beyond the scope of this report. Independent of the interpretation of the spectral shape, these data provide a precise measure of the strong scatter effects on phase at frequencies of interest to communications. Furthermore, they present guidelines with which to test the validity of future strong scatter theory and simulations of phase behavior.

SECTION 4

CONCLUSIONS

We have addressed the question of phase spectral shape in the 10 km to 0.1 km spatial scale regime, under weak and strong scattering conditions. We used multifrequency complex signal data from equatorial observations of the DNA Wideband satellite, that we have reprocessed using current HILAT analysis techniques. The purpose of the study was twofold: (1) to characterize the two-component phase spectral form in weak scatter, which can be simply related to in situ irregularity structure, and (2) to obtain estimates of the effects of diffraction on the phase spectrum during strong scatter.

We have found that a useful weak scatter range corresponds to intensity scintillation levels up through $S_4 \sim 0.5$. Up to this level, diffraction errors are much less than a radian, and the phase spectral shapes are consistent and independent of carrier frequency. The average two-component phase spectrum has a low frequency dependence near $f^{-2.3}$ and a high frequency dependence near $f^{-3.9}$, separated by a break in the spectrum near 650 m. Two-component and power-law spectra comprise the bulk of the weak scatter data; of these, the two-component form is more prevalent. Most of the weak scatter data at UHF show Fresnel nulls, and it is essential that these be avoided in order to obtain accurate measures of the in situ spectral indices.

From our strong scatter analysis, we have estimated the effects of diffraction on the phase signal and on the phase spectrum. Using closely spaced carriers from Wideband, the nature of diffraction effects on the phase signal have been determined. Diffraction contamination for any signal depends most critically upon the minor details of its intensity fading pattern. Quantitative estimates of diffraction contamination show that even between closely spaced carriers, differential structure will

occur at moderate scintillation levels. As for the overall effects of diffraction on the phase spectrum, we have obtained average strong scatter spectral shapes as a function disturbance level. There is evidence in these data of a carrier dependence of phase spectral form. We attribute this dependence to the coincidence of Fresnel and freezing scales at UHF, and their separation at VHF.

Ultimately, the propagation results presented here must be used to make predictions/extrapolations to the nuclear disturbed environment. This involves some key assumptions that must be addressed in future work. One is the degree to which the phase spectral shape directly reflects in situ structure. This report, for the first time, has addressed questions of diffraction contamination as a function of S_4 value. The ultimate test, however, is comparison with in situ observations. Equatorial in situ data from different altitudes will also shed light on the validity of a single thin screen interpretation of an integrated measurement.

Another outstanding issue is the universal applicability of the two-component spectral model refined here for the equator. Since the physical processes involved in determining the spectral slopes have not been specifically identified, it is crucial that convective structure be examined under other conditions; e.g., at high latitudes. We intend to elucidate these issues under continuing DNA support.

32

SECTION 5

LIST OF REFERENCES

1   Rino, C. L. "A Power Law Phase Screen Model for Ionospheric Scintillation 1. Weak Scatter," Radio Sci., 14, 6, 1135-1145 (1979).

2   Livingston, R. C., C. L. Rino, J. P. McClure, and W. B. Hanson, "Spectral Characteristics of Medium-Scale Equatorial F-Region Irregularities," J. Geophys. Res., 86, 2421-2428 (1981).

3   Livingston, R. C., "Comparison of Multifrequency Equatorial Scintillation: American and Pacific Sectors,: Radio Sci., 15, 801-814 (1980).

4   Rino, C. L., R. T. Tsunoda, J. Petriceks, R. C. Livingston, M. C. Kelley, and K. D. Baker, "Simultaneous Rocket-Borne Beacon and In Situ Measurements of Equatorial Spread F--Intermediate Wavelength Results," J. Geophys. Res., 86, 2411-2420 (1981).

5   Rino, C. L., and J. Owen, "On the Temporal Coherence Loss of Strongly Scintillating Signals," Radio Sci., 16, 31-33 (1981).

6   Booker, H. G., and G. Majidiahi, "Theory of Refractive Scattering in Scintillation Phenomena," J. Atmos. Terr. Phy., 43, 1199-1214 (1981).

7   Rino, C. L., and J. Owen, "Numerical Simulations of Intensity Scintillation Using the Power-Law Phase Screen Model," Radio Sci., 19, 891-908 (1984).

8   Buckley, R., "Diffraction by a Random Phase-Changing Screen: A Numerical Experiment," J. Atmos. Terr. Phy., 37, 1431-1446 (1975).

9   Franke, S. J., and C. H. Liu, "Observations and Modeling of Multi-Frequency VHF and Gigahertz Scintillations in the Equatorial Region," J. Geophys. Res., 88, 7075-7085 (1983).

10 Rino, C. L., private communication (1986).

DISTRIBUTION LIST

DEPARTMENT OF DEFENSE

DEFENSE INTELLIGENCE AGENCY
    ATTN: RTS-2B

DEFENSE NUCLEAR AGENCY
    ATTN: NANF
    ATTN: NAWE
    ATTN: OPNA
3 CYS ATTN: RAAE
    ATTN: RAAE K SCHWARTZ
    ATTN: RAAE T WALSH
    ATTN: RAEE
4 CYS ATTN: TITL

DEFENSE TECHNICAL INFORMATION CENTER
12 CYS ATTN: DD

DEPARTMENT OF THE ARMY

U S ARMY NUCLEAR & CHEMICAL AGENCY
    ATTN: LIBRARY

DEPARTMENT OF THE NAVY

NAVAL OCEAN SYSTEMS CENTER
    ATTN: CODE 532
    ATTN: CODE 54 J FERGUSON

DEPARTMENT OF THE AIR FORCE

AIR FORCE WEAPONS LABORATORY, NTAAB
    ATTN: NTN
    ATTN: SUL

DEPARTMENT OF ENERGY

LOS ALAMOS NATIONAL LABORATORY
    ATTN: D SAPPENFIELD
    ATTN: D SIMONS
    ATTN: J WOLCOTT
    ATTN: MS J ZINN
    ATTN: R JEFFRIES
    ATTN: R W WHITAKER
    ATTN: T KUNKLE

SANDIA NATIONAL LABORATORIES
    ATTN: A D THORNBROUGH
    ATTN: D DAHLGREN
    ATTN: ORG 1231 T P WRIGHT
    ATTN: ORG 314 W D BROWN
    ATTN: ORG 332 R C BACKSTROM
    ATTN: SPACE PROJECT DIV
    ATTN: TECH LIB 3141 (RPTS RECEIVING CLRK)

DEPARTMENT OF DEFENSE CONTRACTORS

BERKELEY RSCH ASSOCIATES, INC
    ATTN: C PRETTIE
    ATTN: J WORKMAN
    ATTN: S BRECHT

EOS TECHNOLOGIES, INC
    ATTN: B GABBARD
    ATTN: W LELEVIER

JAYCOR
    ATTN: J SPERLING

KAMAN TEMPO
    ATTN: B GAMBILL
    ATTN: DASIAC
    ATTN: R RUTHERFORD
    ATTN: W MCNAMARA

KAMAN TEMPO
    ATTN: DASIAC

MAXIM TECHNOLOGIES, INC
    ATTN: J LEHMAN
    ATTN: J MARSHALL
    ATTN: J SO
    ATTN: N CIANOS

MISSION RESEARCH CORP
    ATTN: B R MILNER
    ATTN: C LAUER
    ATTN: C RINO
    ATTN: D ARCHER
    ATTN: D KNEPP
    ATTN: F FAJEN
    ATTN: F GUIGLIANO
    ATTN: G MCCARTOR
    ATTN: R BIGONI
    ATTN: R BOGUSCH
    ATTN: R DANA
    ATTN: R HENDRICK
    ATTN: R KILB
    ATTN: R MORGANSTERN
    ATTN: S GUTSCHE
    ATTN: TECH LIBRARY

PACIFIC-SIERRA RESEARCH CORP
    ATTN: E FIELD JR
    ATTN: F THOMAS
    ATTN: H BRODE, CHAIRMAN SAGE

PHYSICAL RESEARCH, INC
    ATTN: R DELIBERIS
    ATTN: T STEPHENS

PHYSICAL RESEARCH, INC
    ATTN: J DEVORE
    ATTN: J THOMPSON
    ATTN: W SCHLUETER

R & D ASSOCIATES
    ATTN: B LAMB
    ATTN: C GREIFINGER
    ATTN: F GILMORE
    ATTN: G HOYT
    ATTN: H ORY
    ATTN: M GANTSWEG
    ATTN: M GROVER
    ATTN: R TURCO
    ATTN: W KARZAS

SCIENCE APPLICATIONS INTL CORP
    ATTN: C SMITH
    ATTN: D HAMLIN

SRI INTERNATIONAL
    ATTN: D MCDANIEL
2 CYS ATTN: R LIVINGSTON
2 CYS ATTN: T DABBS
    ATTN: W CHESNUT
    ATTN: W JAYE

TOYON RESEARCH CORP
    ATTN: J GARBARINO
    ATTN: J ISE

VISIDYNE, INC
    ATTN: J CARPENTER

END

7-87

DTIC